An ultrasonic frequency sweep interferometer for liquids at high temperature: 1. Acoustic model

Yuhui Ai and Rebecca Lange

Department of Geological Sciences, University of Michigan, Ann Arbor, Michigan, USA

Received 11 October 2003; revised 16 April 2004; accepted 12 May 2004; published 4 December 2004.

[1] A general acoustic model for a frequency sweep rod-liquid-rod interferometer applicable to high-temperature silicate liquids is presented. The wave propagations in the acoustic model are solved according to the accurate elastic wave equation and the acoustic wave equation. The solutions indicate that when a pulsed wave is sent down a buffer rod, which is partially immersed in a silicate liquid, the return signal consists of a series of plane waves (mirror reflections from the liquid) and two series of interfering pulses (modes A and B), which are propagating disturbances guided by the cylindrical surface of the upper rod. The acoustic model gives mathematical expressions for the time delays between the various interfering pulses and between the mirror reflections, which are predicted to vary according to the material and dimensions of the upper buffer rod and liquid. These predictions are verified by experiments on molybdenum and aluminum rods of varying dimensions in air, water, and silicate liquid. These results demonstrate that mirror reflections from the liquid can be isolated from the interfering pulses in the return signal by appropriate choice of the dimensions and material of the upper rod. This theoretical model provides a critical foundation for construction of an acoustic interferometer that is uniquely able to measure relaxed sound speeds in silicate liquids at high temperature and high pressure by the frequency sweep method. *INDEX TERMS:* 3994 Mineral Physics: Instruments and techniques; 3919 Mineral Physics: Equations of state; 3939 Mineral Physics: Physical thermodynamics; 3999 Mineral Physics: General or miscellaneous; 5102 Physical Properties of Rocks: Acoustic properties; *KEYWORDS:* ultrasonic interferometer, sound speed, silicate liquids

Citation: Ai, Y., and R. Lange (2004), An ultrasonic frequency sweep interferometer for liquids at high temperature: 1. Acoustic model, *J. Geophys. Res.*, *109*, B12203, doi:10.1029/2003JB002842.

1. Introduction

[2] An equation of state (P-V-T relation) for magmatic liquids is a prerequisite for quantitative models of partial melting and subsequent melt transport in the Earth and other planetary bodies. Although the systematics of silicate melt density with composition and temperature are fairly well established at one bar, the compressional properties are less well known. An outstanding question is how melt compressibility (β) or bulk modulus ($K = 1/\beta$) changes with pressure, which is referred to as K' ($=dK/dP$). Most of our information on K' is from sink/float and shock wave experiments on a relatively narrow set of liquids [e.g., *Agee and Walker*, 1993; *Chen et al.*, 2002], and there is not yet a predictive model for how K' varies systematically with melt composition. Moreover, there are not any compressibility measurements on silicate liquids with dissolved volatiles, despite the necessity of these data for accurate thermodynamic calculations of volatile solubility in magmatic melts at high pressure.

[3] One of the most direct methods for obtaining melt compressibility is through measurements of sound speed via acoustic interferometry. In theory, this technique can be applied to silicate melts either by varying the path length or the frequency of the acoustic wave through the melt. The variable path length (VPL) interferometric technique has long been applied to silicate melts of geological relevance [*Katahara et al.*, 1981; *Rivers and Carmichael*, 1987; *Kress et al.*, 1988; *Secco et al.*, 1991; *Webb and Courtial*, 1996], but all experiments to date have been limited to atmospheric pressure. The primary limitation of the VPL method for use at high pressure (e.g., in an internally heated pressure vessel) is that it requires mechanical movement of the buffer rod, which is easily performed at 1 bar but is extremely difficult under in situ high-pressure conditions.

[4] *Katahara et al.* [1981] used an acoustic ray model to propose that sound speed measurements on silicate melts could be performed alternatively by fixing path length and varying the frequency of the acoustic wave. We refer to this approach as frequency sweep (FS) acoustic interferometry to distinguish it from the VPL method. Although FS interferometry has been successfully applied to high-pressure crystalline phases, the relatively high frequencies and broad intervals employed (e.g., 10–70 MHz [*Li et al.*, 1996, 1998] and 300–1200 MHz [*Shen et al.*, 1998]) cannot be used for silicate melts. For liquids the timescale of the

0148-0227/04/2003JB002842$09.00

sound speed measurements must be longer than that for structural relaxation. Practically, for most silicate liquid compositions between 1000 and 1600°C this requires measurements in the 3–12 MHz range. Additionally, in order to test whether liquid sound velocity data are relaxed, a series of measurements at different frequencies must be performed to evaluate whether the sound speed is frequency-independent. Therefore, in order to apply the FS method to silicate liquids the frequency interval must be relatively narrow (1–2 MHz instead of tens to hundreds of megahertz) and the centered frequencies must be low (<10 MHz). The best way to meet this requirement for liquids is not to vary the carrier frequency transmitted down the rod (as done in the FS method applied to minerals) but instead to send a fixed frequency, wideband (1–2 MHz), short pulse (~1 μs) down the buffer rod and then perform a Fourier transform on the echo in order to analyze the frequency response. However, this approach requires a rigorous understanding of the entire return signal so that any interfering pulses can be eliminated.

[5] To date, only an acoustic ray model has been developed to interpret high-temperature, acoustic interferometry [*Katahara et al.*, 1981; *Rivers*, 1985], which deals with reflection and transmission in such a way that only propagation of the plane waves are considered in the buffer rod and in the liquid. Theoretically, the acoustic ray model is only applicable to cases where the radius of the buffer rod is much smaller than the wavelength of the longitudinal wave [*Graff*, 1975; *Billingham and King*, 2000; *Kingsler*, 2000; *Mason*, 1958; *Soutas-Little*, 1999; *Achenbach*, 1973]. Thus, for ultrasonic frequencies from 3 to 12 MHz (the range required for silicate liquids) the radius of a molybdenum buffer rod, for example, must be much smaller than 0.3 mm, which is too narrow to be used in a feasible design. Use of a buffer rod with a significantly larger diameter leads to a returned signal that consists of a train of echoes that are out of phase.

[6] For example, *Rivers* [1985] reported that if a single ultrasonic pulse is transmitted down a smooth buffer rod of 1.3 cm diameter, then the returned signal includes a series of interfering pulses that must be eliminated for successful implementation of the VPL method. *Rivers* [1985] interpreted these echoes as reflections off the outside surface of the smooth rod, and he noted that if the outside of the rod is knurled over its length, then the extraneous echoes are eliminated, and a single sharp signal is returned. However, it is important to point out that knurling the rod only eliminates the interfering pulses at select frequencies and not for all frequencies. Because a continuum of frequencies is used for the FS method, knurling the rod will offer no improvement and instead may introduce scattering waves that complicate interpretation of the return signal.

[7] In this paper, we show that the interfering pulses are not reflections but instead are nondispersive waves with properties that are primarily determined by the dimension and elastic properties of the buffer rod material; only their bandwidths are restricted by the transmitted signal. These interfering pulses are poorly correlated with the transmitted signal and thus cannot be interpreted as reflections of the excitation wave. They are best thought of as propagating disturbances guided by the cylindrical surface of the rod, which arise owing to a complicated interaction of the body waves of an infinite medium with the cylindrical surface. Therefore, before further progress can be made on developing a FS interferometer adaptable to silicate melts at high pressure, a complete theoretical analysis of the general acoustic model of the FS interferometer and solutions to the wave equations generated in this model must be performed and tested experimentally. This is the primary goal of this study (part 1), which is the first in a sequence of two related papers. In part 2 [*Ai and Lange*, 2004] we describe the mechanical assembly and signal-processing algorithm for the new FS interferometer that we have designed, and we illustrate its precision and accuracy when applied to high-temperature melts at 1 bar.

2. Acoustic Model of the Interferometer

[8] The general acoustic model is for a rod-liquid-rod (RLR) configuration (as shown in Figure 1) in cylindrical polar coordinates [*Billingham and King*, 2000]. Both the upper and lower rods are ideal semi-infinite cylindrical bars with radius a. In practice, because the transmitted pulse is designed to be short relative to the length of the rod, the acoustic reflections from the upper end of the upper rod and the lower end of the lower rod are all separated far away in time from the useful signal. As a result, the two boundaries have no impact on the general results of the model. For signal-processing purposes they can be neglected and considered to be at $z = -\infty$, $z = +\infty$ for simplicity. The assumption of the same radius for the two buffer rods also makes no difference in the final signal-processing procedures. As for the liquid, because it is housed in a cylindrical crucible, the model must be a finite circular waveguide [*Billingham and King*, 2000] with a thickness S and solid circumferential boundaries marked by the dark lines in Figure 1. Here, because measurements are made on relaxed liquids (and tested by making measurements at different centered frequencies; see part 2), viscosity need not be considered in the model.

[9] The response of the RLR to an acoustic load $s(t)$ in the upper rod (Figure 1) provides essential information on the sound speed in the liquid. Instead of a ray model, wave equations and their solutions are pursued here for theoretical completeness. The vibrations or displacements of particles in the rods and liquid are governed by Navier's equation and the general linear acoustic wave equation, respectively. In the rods the three-dimensional wave is described in terms of cylindrical polar coordinates by the displacement components in the z *axis* direction, $w(r, \theta, z, t)$, the radial direction, $u(r, \theta, z, t)$, and the circumferential direction, $v(r, \theta, z, t)$ [*Billingham and King*, 2000]. In the liquid the displacement is obtained from the velocity potential, $\psi(r, \theta, z, t)$ [*Billingham and King*, 2000]. To solve for the entire acoustic fields in the RLR model, boundary conditions are applied. To avoid unnecessary complexity, it is assumed that the acoustic field is symmetric about the z axis and that both the rods and liquid are perfectly shaped; thus the acoustic fields in the RLR model are not only independent of angle θ, but $v(r, \theta, z, t)$ vanishes as well. In addition, the boundary between the upper rod and liquid is coordinated at $z = 0$. In

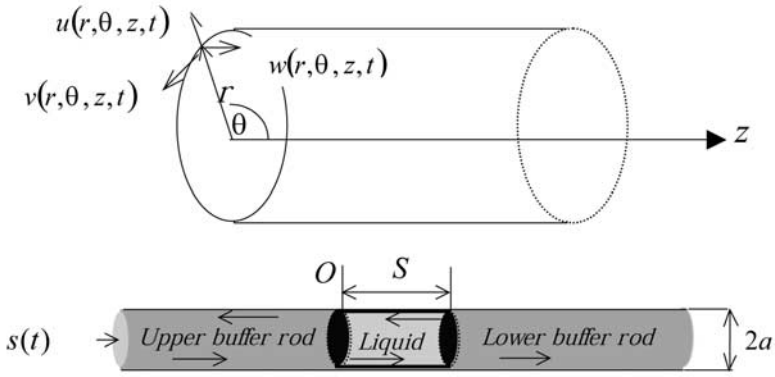

Figure 1. Schematic diagram illustrating the rod-liquid-rod (RLR) model in cylindrical polar coordinates. This is a one-transducer configuration where the ultrasonic wave is transmitted and received by the same transducer. Mathematically, the acoustic source (also the receiver) is located at negative infinity in z axis; however, physically the transducer is mounted on the top of the upper buffer rod.

the text below, we first examine the propagation of a continuous wave (CW) in both rods and the liquid so that the acoustic fields in the FS interferometer can be solved. Next, we discuss the propagation of a pulsed wave, upon which our signal processing can be performed.

3. Propagation of a Continuous Wave in a Semi-Infinite Rod

[10] In each rod, Navier's equation in cylindrical polar coordinates is employed [*Billingham and King*, 2000]. In Figure 1, with Helmholtz representation, where $H = (0, \varphi(r, z, t), 0)$ and $\phi = \phi(r, z, t)$ [*Aris*, 1962; *Graff*, 1975; *Billingham and King*, 2000; *Chou*, 1992; *Farlow*, 1993], the displacements can be expressed as

$$u = \frac{\partial \phi}{\partial r} - \frac{\partial \varphi}{\partial z}, w = \frac{\partial \phi}{\partial z} + \frac{1}{r}\frac{\partial}{\partial r}(r\varphi), \tag{1}$$

where ϕ and φ represent two different potential functions. Thus the Navier's equations take the following simplified forms [*Billingham and King*, 2000; *Nagy*, 1995]:

$$\begin{aligned} \frac{\partial^2 \phi}{\partial r^2} + \frac{1}{r}\frac{\partial \phi}{\partial r} + \frac{\partial^2 \phi}{\partial z^2} &= \frac{1}{c_1^2}\frac{\partial^2 \phi}{\partial t^2} \\ \frac{\partial^2 \varphi}{\partial r^2} + \frac{1}{r}\frac{\partial \varphi}{\partial r} + \frac{\partial^2 \varphi}{\partial z^2} - \frac{\varphi}{r^2} &= \frac{1}{c_2^2}\frac{\partial^2 \varphi}{\partial t^2}, \end{aligned} \tag{2}$$

where c_1 and c_2 are the speeds of the dilatational and rotational waves, respectively, in an infinite elastic body. Owing to the cross sections at $z = 0$ and $z = S$, reflections are introduced in the upper rod, standing waves occur in the liquid, and one-way propagation exists in the lower rod. According to *Graff* [1975] and *Billingham and King* [2000] the general solutions of equation (2) in the upper rod to a CW load of $s(t) = e^{j\omega t}$ take the forms

$$\begin{aligned} \phi_{(u)}(r, z, t) &= AJ_0(pr)\left(\beta e^{jkz} + e^{-jkz}\right)e^{j\omega t} \\ \varphi_{(u)}(r, z, t) &= BJ_1(sr)\left(\gamma e^{jkz} + e^{-jkz}\right)e^{j\omega t}, \end{aligned} \tag{3}$$

where ω is angular frequency, j represents imaginary number unit, and $J_1(x)$ and $J_0(x)$ are Bessel functions of the first kind of order 1 and order 0, respectively [*Bronshtein and Semendyayev*, 1998]; A and B are constants; β and γ are reflection coefficients; s and p are coefficients, and the wave number k is determined by

$$k^2 = \left(\frac{\omega^2}{c_2^2} - s^2\right) = \left(\frac{\omega^2}{c_1^2} - p^2\right). \tag{4}$$

In the lower rod, however, the general solutions are of one-way propagation:

$$\begin{aligned} \phi_{(l)}(r, z, t) &= CJ_0(gr)e^{-j\eta(z-S)}e^{j\omega t} \\ \varphi_{(l)}(r, z, t) &= DJ_1(qr)e^{-j\eta(z-S)}e^{j\omega t}, \end{aligned} \tag{5}$$

where g and q are coefficients and η is the wave number. Here C and D are transmission coefficients, and the wave number is determined by

$$\eta^2 = \left(\frac{\omega^2}{c_2^2} - q^2\right) = \left(\frac{\omega^2}{c_1^2} - g^2\right). \tag{6}$$

From equations (1) and (3) the general solutions in the upper rod are

$$\begin{aligned} u_{(u)} &= \left\{[-ApJ_1(pr) + jkBJ_1(sr)]e^{-jkz} \right. \\ &\quad \left. + [-Ap\beta J_1(pr) - jkBJ_1(sr)\gamma]e^{jkz}\right\}e^{j\omega t} \\ w_{(u)} &= \left\{[-AjkJ_0(pr) + BsJ_0(sr)]e^{-jkz} \right. \\ &\quad \left. + [AjkJ_0(pr)\beta + BsJ_0(sr)\gamma]e^{jkz}\right\}e^{j\omega t}. \end{aligned} \tag{7}$$

In the lower rod they are

$$\begin{aligned} u_{(l)} &= [-CgJ_1(gr) + j\eta DJ_1(qr)]e^{-j\eta(z-S)}e^{j\omega t} \\ w_{(l)} &= [-Cj\eta J_0(gr) + DqJ_0(qr)]e^{-j\eta(z-S)}e^{j\omega t}. \end{aligned} \tag{8}$$

To find p, s, g, and q, stress-free boundary conditions on the circumferential surface and on the two cross sections are applied. In the upper rod,

$$\sigma_{rr} = \left[\lambda\Delta + 2\mu\frac{\partial u}{\partial r}\right]_{r=a} = 0, \quad \sigma_{rz} = \mu\left[\frac{\partial u}{\partial z} + \frac{\partial w}{\partial r}\right]_{r=a} = 0, \tag{9}$$

$$\sigma_{zr} = \mu\left[\frac{\partial u}{\partial z} + \frac{\partial w}{\partial r}\right]_{z=0} = 0, \tag{10}$$

where σ_{rr} is normal stress on the circumferential surface and σ_{rz}, σ_{zr} are shear stresses,

$$\Delta = \frac{\partial u}{\partial r} + \frac{u}{r} + \frac{\partial w}{\partial z}$$

[*Billingham and King*, 2000], $u = u_{(u)}$, $w = w_{(u)}$ and $\lambda = \lambda_{(u)}$, $\mu = \mu_{(u)}$ are the Lame constants of the upper rod. Therefore solving equations (9) and (10) yields

$$\begin{aligned}
&\left\{\frac{p}{a}J_1(pa) - \frac{1}{2}(s^2 - k^2)J_0(pa)\right\}A \\
&\quad + \left\{-\frac{jk}{a}J_1(sa) + jksJ_0(sa)\right\}B = 0, \\
&\left\{\frac{p}{a}J_1(pa) - \frac{1}{2}(s^2 - k^2)J_0(pa)\right\}A\beta \\
&\quad + \left\{\frac{jk}{a}J_1(sa) - jksJ_0(sa)\right\}B\gamma = 0, \\
&2jkpJ_1(pa)A - (s^2 - k^2)J_1(sa)B = 0, \\
&-2jkpJ_1(pa)A\beta - (s^2 - k^2)J_1(sa)B\gamma = 0, \\
&2jkpJ_1(pr)A - (s^2 - k^2)J_1(sr)B = 0, \\
&-2jkpJ_1(pr)A\beta - (s^2 - k^2)J_1(sr)B\gamma = 0.
\end{aligned} \tag{11}$$

From equation (11) the boundary conditions can be reduced to

$$\begin{aligned}
&\beta = -\gamma, \\
&\left\{\frac{p}{a}J_1(pa) - \frac{1}{2}(s^2 - k^2)J_0(pa)\right\}A \\
&\quad + \left\{-\frac{jk}{a}J_1(sa) + jksJ_0(sa)\right\}B = 0, \\
&\quad 2jkpJ_1(pr)A - (s^2 - k^2)J_1(sr)B = 0, \qquad 0 \le r \le a.
\end{aligned} \tag{12}$$

Thus, in the upper rod,

$$\begin{aligned}
u_{(u)} &= [-ApJ_1(pr) + jkBJ_1(sr)]\{e^{-jkz} + \beta e^{jkz}\}e^{j\omega t} \\
w_{(u)} &= [-AjkJ_0(pr) + BsJ_0(sr)]\{e^{-jkz} - \beta e^{jkz}\}e^{j\omega t}.
\end{aligned} \tag{13a}$$

Similarly, in the lower rod,

$$\begin{aligned}
u_{(l)} &= [-CpJ_1(pr) + jkDJ_1(sr)]e^{-jk(z-S)}e^{j\omega t} \\
w_{(l)} &= [-CjkJ_0(pr) + DsJ_0(sr)]e^{-jk(z-S)}e^{j\omega t}.
\end{aligned} \tag{13b}$$

Next, the values for s, p, and k and then A, B, C, and D must be obtained. In both rods, in order to find s, p, and k, two cases need to be considered without any loss of mathematical generality.

3.1. Case 1: $A \neq 0$ (Mode A)

[11] The waves corresponding to $A \neq 0$ are defined here as waves of mode A. To find them, the boundary conditions in equation (12) must be changed slightly to avoid unnecessary mathematical complexity [*Davies*, 1948; *Mason*, 1965; *Thurston*, 1978]. In equation (12), instead of setting the boundary conditions identical to zero, they are set to be close to zero. This adjustment leads to the most important class of wave propagations that are observed in our experiments, which are described below. Without this slight adjustment of the boundary conditions the experimental results (discussed in detail below) cannot otherwise be explained mathematically. From equation (12), all possible combinations of solutions can be included in the following three cases:

[12] 1. Case for $B \neq 0$ and

$$\left\{-\frac{jk}{a}J_1(sa) + jksJ_0(sa)\right\} \neq 0;$$

thus

$$\begin{aligned}
&p\left\{\frac{J_1(pa)}{a} - \frac{jkJ_1(pa)A}{J_1(sa)B}J_0(pa)\right\}A \\
&\quad + \left\{-\frac{jk}{a}J_1(sa) + jksJ_0(sa)\right\}B \approx 0
\end{aligned} \tag{14a}$$

$$A2jkpJ_1(pr) - (s^2 - k^2)J_1(sr)B \approx 0. \tag{14b}$$

Therefore the solution is

$$B \approx 0 \text{ or } A \gg B; p = 0 \Rightarrow k = \frac{\omega}{c_1}, s = \sqrt{\left(\frac{\omega}{c_2}\right)^2 - \left(\frac{\omega}{c_1}\right)^2}. \tag{14c}$$

[13] 2. Case for $B = 0$; thus

$$\begin{aligned}
&\left\{\frac{p}{a}J_1(pa) - \frac{1}{2}(s^2 - k^2)J_0(pa)\right\}A = 0 \\
&\qquad 2jkpJ_1(pr)A = 0.
\end{aligned} \tag{15}$$

This requires that

$$p = 0, s = k \Rightarrow k = \frac{\omega}{c_1}, s = \sqrt{\left(\frac{\omega}{c_2}\right)^2 - \left(\frac{\omega}{c_1}\right)^2}, \left(\frac{\omega}{c_1}\right)^2 = \frac{1}{2}\left(\frac{\omega}{c_2}\right)^2. \tag{16}$$

However, since $(\omega/c_1)^2 < \frac{1}{2}(\omega/c_2)^2$ [*Billingham and King*, 2000], equation (16) cannot be satisfied, and this solution must be eliminated.

[14] 3. Case for $B \neq 0$ and

$$\left\{-\frac{jk}{a}J_1(sa) + jksJ_0(sa)\right\} = 0;$$

thus

$$p\left\{\frac{J_1(pa)}{a} - \frac{jkJ_1(pa)A}{J_1(sa)B}J_0(pa)\right\}A = 0. \tag{17}$$

$$A2\,jkpJ_1(pr) - \left(s^2 - k^2\right)J_1(sr)B \approx 0.$$

Since s cannot be zero, the solution is

$$A \gg B,\ \ B \approx 0;\ p = 0 \Rightarrow k = \frac{\omega}{c_1}, s = \sqrt{\left(\frac{\omega}{c_2}\right)^2 - \left(\frac{\omega}{c_1}\right)^2},$$
$$J_1'(sa) = 0. \tag{18}$$

(Here $s \neq k$ for the same reason as that in case 2.)

[15] To make $J_1'(sa) = 0$, it is required that

$$s_i = \frac{r_i}{a} \Rightarrow \omega_i = \frac{c_1 r_i}{a\sqrt{(c_1/c_2)^2 - 1}}, k_i = \frac{\omega_i}{c_1}, i = 0 \ldots \infty, \tag{19}$$

where r_i are the roots of $J_1'(x) = 0$ and ω_i are defined as the eigenfrequencies of mode A.

[16] Equation (19) shows that if the transmitted frequency is equal to one of the eigenfrequencies, besides equation (14c), solution (19) should be added to the entire solution. Thus the analytical expression of mode A is

$$\begin{aligned} u_{(u,A)} = {} & j\frac{\omega}{c_1}BJ_1\left(r\sqrt{\left(\frac{\omega}{c_2}\right)^2 - \left(\frac{\omega}{c_1}\right)^2}\right)\left\{\exp\left[j\omega\left(t - \frac{z}{c_1}\right)\right]\right. \\ & \left. + \beta_A \exp\left[j\omega\left(t + \frac{z}{c_1}\right)\right]\right\} \\ & + \sum_{i=0}^{\infty}\delta\left(\omega - \frac{c_1 r_i}{a\sqrt{(c_1/c_2)^2 - 1}}\right)\left[\frac{jr_i B_{(i,A)}}{a\sqrt{(c_1/c_2)^2 - 1}}J_1\left(r\frac{r_i}{a}\right)\right] \\ & \cdot \left\{\exp\left[j\frac{c_1 r_i}{a\sqrt{(c_1/c_2)^2 - 1}}\left(t - \frac{z}{c_1}\right)\right]\right. \\ & \left. + \beta_{(i,A)}\exp\left[j\frac{c_1 r_i}{a\sqrt{(c_1/c_2)^2 - 1}}\left(t + \frac{z}{c_1}\right)\right]\right\} \end{aligned} \tag{20a}$$

$$\begin{aligned} w_{(u,A)} = {} & \left\{-Aj\frac{\omega}{c_1} + B\sqrt{\left(\frac{\omega}{c_2}\right)^2 - \left(\frac{\omega}{c_1}\right)^2}\cdot J_0\left(r\sqrt{\left(\frac{\omega}{c_1}\right)^2 - \left(\frac{\omega}{c_2}\right)^2}\right)\right\} \\ & \cdot \left\{e^{j\omega\left(t - \frac{z}{c_1}\right)} - \beta_A e^{j\omega\left(t + \frac{z}{c_1}\right)}\right\} \\ & + \sum_{i=0}^{\infty}\delta\left(\omega - \frac{c_1 r_i}{a\sqrt{(c_1/c_2)^2 - 1}}\right)\left[\frac{B_{(i,A)}r_i}{a}J_0\left(r\frac{r_i}{a}\right)\right] \\ & \cdot \left\{\exp\left[j\frac{c_1 r_i}{a\sqrt{(c_1/c_2)^2 - 1}}\left(t - \frac{z}{c_1}\right)\right]\right. \\ & \left. - \beta_{(i,A)}\exp\left[j\frac{c_1 r_i}{a\sqrt{(c_1/c_2)^2 - 1}}\left(t + \frac{z}{c_1}\right)\right]\right\}, \end{aligned} \tag{20b}$$

where $A \gg B$, $A \gg B_{(i,A)}$, $B \approx 0$, $B_{(i,A)} \approx 0$. The parameter $\beta_{(i,A)}$ are constants corresponding to ω_i in equation (19), and

$$\delta(\omega - \omega_i) = 0; \qquad \omega \neq \omega_i$$
$$\delta(\omega - \omega_i) = 1; \qquad \omega = \omega_i.$$

Solution (20) shows that mode A travels with group velocity c_1, the same as that of longitudinal wave, and is thus nondispersive. This property will be used to accomplish the measurement of sound speeds in silicate melts (discussed in part 2).

3.2. Case 2: $A = 0$ (Mode B)

[17] The waves corresponding to $A = 0$ are defined here as waves of mode B. From equation (12),

$$\left(s^2 - k^2\right) = 0,\ \left\{-\frac{jk}{a}J_1(sa) + jksJ_0(sa)\right\} = 0. \tag{21a}$$

Thus

$$k = s = \frac{\omega}{\sqrt{2}c_2},\ \left\{-\frac{J_1(sa)}{a} + sJ_0(sa)\right\} = 0. \tag{21b}$$

Since $k = s \neq 0$ (otherwise, $u = w = 0$), it follows that

$$J_1'\left(\frac{\omega}{\sqrt{2}c_2}a\right) = 0 \Rightarrow k_i = s_i = \frac{r_i}{a}, \quad \omega_i = \frac{r_i\sqrt{2}c_2}{a}, i = 0, \ldots \infty, \tag{22}$$

where ω_i are defined as the eigenfrequencies of mode B. Equations (21)–(22) show that if the transmitted frequency is equal to one of the eigenfrequencies of

mode B, mode B will be excited. The expression of mode B is

$$u_{(u,B)} = \sum_{i=0}^{\infty} \delta\left(\omega - \frac{r_i\sqrt{2}c_2}{a}\right)\left[jB_{(i,B)}\frac{r_i}{a}J_1\left(\frac{r_i}{a}r\right)\right] \cdot \left\{\exp\left[j\frac{r_i}{a}\left(\sqrt{2}c_2t - z\right)\right] + \beta_{(i,B)}\exp\left[j\frac{r_i}{a}\left(\sqrt{2}c_2t + z\right)\right]\right\} \tag{23a}$$

$$w_{(u,B)} = \sum_{i=0}^{\infty} \delta\left(\omega - \frac{r_i\sqrt{2}c_2}{a}\right)\left[B_{(i,B)}\frac{r_i}{a}J_0\left(\frac{r_i}{a}r\right)\right] \cdot \left\{\exp\left[j\frac{r_i}{a}\left(\sqrt{2}c_2t - z\right)\right] - \beta_{(i,B)}\exp\left[j\frac{r_i}{a}\left(\sqrt{2}c_2t + z\right)\right]\right\}, \tag{23b}$$

where $\beta_{(i,B)}$ are constants corresponding to ω_i in equation (22). Examination of equation (23) shows that waves of mode B are nondispersive and have a group velocity of $\sqrt{2}c_2$. Since $\sqrt{2}c_2 < c_1$, in most pulse cases, waves of mode B can be separated in time from those of mode A, which reduces the complexity of signal processing.

3.3. Entire Solution (Cases 1 and 2)

[18] The entire solution is the addition of waves of mode A and those of mode B. Therefore, in the upper rod,

$$u_{(u)} = u_{(u,A)} + u_{(u,B)} \tag{24a}$$

$$w_{(u)} = w_{(u,A)} + w_{(u,B)}. \tag{24b}$$

Similarly, in the lower rod,

$$u_{(l)} = \exp\left[j\omega\left(t - \frac{z-S}{c_1}\right)\right]\left\{\left[j\frac{\omega}{c_1}DJ_1\left(r\sqrt{\left(\frac{\omega}{c_2}\right)^2 - \left(\frac{\omega}{c_1}\right)^2}\right)\right] + \sum_{i=0}^{\infty}\delta\left(\omega - \frac{c_1r_i}{a\sqrt{(c_1/c_2)^2-1}}\right)\left[j\frac{r_i}{a\sqrt{(c_1/c_2)^2-1}}D_{(i,A)}J_1\left(r\frac{r_i}{a}\right)\right]\right\} + \sum_{i=0}^{i=\infty}\delta\left(\omega - \frac{r_i\sqrt{2}c_2}{a}\right)\left[j\frac{r_i}{a}D_{(i,B)}J_1\left(\frac{r_i}{a}r\right)\right]\exp\left[j\frac{r_i}{a}\left(\sqrt{2}c_2t - z + S\right)\right] \tag{25a}$$

$$w_{(l)} = \left\{-Cj\frac{\omega}{c_1} + D\sqrt{\left(\frac{\omega}{c_2}\right)^2 - \left(\frac{\omega}{c_1}\right)^2}J_0\left(r\sqrt{\left(\frac{\omega}{c_1}\right)^2 - \left(\frac{\omega}{c_2}\right)^2}\right) + \sum_{i=0}^{\infty}\delta\left(\omega - \frac{c_1r_i}{a\sqrt{(c_1/c_2)^2-1}}\right)D_{(i,A)}\frac{r_i}{a}J_0\left(r\frac{r_i}{a}\right)\right\}\exp\left[j\omega\left(t - \frac{z-S}{c_1}\right)\right] + \sum_{i=0}^{\infty}\delta\left(\omega - \frac{r_i\sqrt{2}c_2}{a}\right)\left[D_{(i,B)}\frac{r_i}{a}J_0\left(\frac{r_i}{a}r\right)\right]e^{j\frac{r_i}{a}\left(\sqrt{2}c_2t - z + S\right)}, \tag{25b}$$

where $C \gg D$, $C \gg D_{(i,A)}$, $D \approx 0$, $D_{(i,A)} \approx 0$.

[19] In summary, from equations (24)–(25), only two kinds of nondispersive wave propagations exist in each rod with group velocities c_1 and $\sqrt{2}c_2$, respectively. The plane wave portions, related to coefficients A and C in equations (20) and (25), constitute most of the wave energy within the rods.

4. Propagation of a Continuous Wave in the Liquid

[20] In a circular waveguide the velocity potential in the liquid [*Billingham and King*, 2000] is

$$\psi(r,z,t) = e^{j\omega t}\sum_{i=0}^{\infty}\left[J_0\left(\frac{\lambda_i}{a}r\right)\left(E_ie^{-j\nu_iz} + F_ie^{j\nu_iz}\right)\right], \tag{26a}$$

where

$$J_1(\lambda_i) = 0,\ i = 0\cdots\infty,$$

$$if\left(\frac{\omega}{c}\right)^2 - \left(\frac{\lambda_i}{a}\right)^2 > 0 \Rightarrow \nu_i = \sqrt{\left(\frac{\omega}{c}\right)^2 - \left(\frac{\lambda_i}{a}\right)^2},\ i = 0\ldots n\ \lambda_0 = 0,$$

$$if\left(\frac{\omega}{c}\right)^2 - \left(\frac{\lambda_i}{a}\right)^2 < 0 \Rightarrow \nu_i = -j\sqrt{\left|\left(\frac{\omega}{c}\right)^2 - \left(\frac{\lambda_i}{a}\right)^2\right|},$$

$$F_i = 0,\ i = n+1\ldots\infty,$$

E_i, F_i are constants, and c is the sound speed of the liquid. The displacement solutions can be obtained from equation (26a):

$$u_{(m)} = \int\frac{\partial\psi}{\partial r}dt \qquad w_{(m)} = \int\frac{\partial\psi}{\partial z}dt \tag{26b}$$

so that

$$u_{(m)} = e^{j\omega t}\sum_{i=0}^{\infty}\left[\frac{\lambda_i}{j\omega\cdot a}\left(-E_ie^{-j\nu_iz} - F_ie^{j\nu_iz}\right)J_1\left(\frac{\lambda_i}{a}r\right)\right]$$
$$w_{(m)} = e^{j\omega t}\sum_{i=0}^{\infty}\left[\frac{\nu_i}{\omega}\left(-E_ie^{-j\nu_iz} + F_ie^{j\nu_iz}\right)J_0\left(\frac{\lambda_i}{a}r\right)\right]. \tag{26c}$$

Using Fourier-Bessel series [*Kovach*, 1982], equation (26c) can be projected over the orthogonal function sets $J_0[(r_i/a)r]$ and $J_1[(r_i/a)r]$ so that

$$J_0\left(\frac{\lambda_i}{a}r\right) = \sum_{n=0}^{\infty}b_{(i,n)}J_0\left(\frac{r_n}{a}r\right), J_1\left(\frac{\lambda_i}{a}r\right) = \sum_{n=0}^{\infty}d_{(i,n)}J_1\left(\frac{r_n}{a}r\right)$$
$$i = 0\ldots\infty,$$

where

$$b_{(i,n)} = \frac{1}{a^2J_0^2(r_n)}\int_0^a rJ_0\left(\frac{\lambda_i}{a}r\right)J_0\left(\frac{r_n}{a}r\right)dr,$$

$$d_{(i,n)} = \frac{2r_n^2}{a^2J_1(r_n^2)(r_n^2-1)}\int_0^a rJ_1\left(\frac{\lambda_i}{a}r\right)J_1\left(\frac{r_n}{a}r\right)dr.$$

Thus

$$u_{(m)} = e^{j\omega t}\sum_{n=0}^{\infty}\left[\sum_{i=0}^{\infty}\frac{\lambda_i d_{(i,n)}}{j\omega a}\left(-E_i e^{-j\nu_i z} - F_i e^{j\nu_i z}\right)\right]J_1\left(\frac{r_n}{a}r\right) \tag{26d}$$

$$w_{(m)} = e^{j\omega t}\sum_{n=0}^{\infty}\left[\sum_{i=0}^{\infty}\frac{\nu_i b_{(i,n)}}{\omega}\left(-E_i e^{-j\nu_i z} + F_i e^{j\nu_i z}\right)\right]J_0\left(\frac{r_n}{a}r\right).$$

5. Propagation of a Continuous Wave in the RLR Model

[21] In order to understand the echo signal in the upper rod the reflection coefficients β_A, $\beta_{(i,A)}$, and $\beta_{(i,B)}$ must be determined. To do so, the continuities of stress and displacement on the boundaries of the cross sections at $z = 0$ and $z = S$ are applied:

$$\sigma_{(zz,u)} = \sigma_{(zz,m)}\big|_{z=0}\ \sigma_{(zz,l)} = \sigma_{(zz,m)}\big|_{z=S}\ w_{(u)} = w_{(m)}\big|_{z=0}\quad w_{(l)} = w_{(m)}\big|_{z=S}, \tag{27a}$$

where $\sigma_{(zz,u)}$, $\sigma_{(zz,m)}$, $\sigma_{(zz,l)}$ are z direction normal stress in the upper rod, liquid, and lower rod, respectively. In both rods and in the liquid the stress along the z direction [*Billingham and King*, 2000] is

$$\sigma_{(zz)} = \lambda\left(\frac{\partial u}{\partial r} + \frac{u}{r} + \frac{\partial w}{\partial z}\right) + 2\mu\frac{\partial w}{\partial z}, \tag{27b}$$

and λ, μ are Lame constants. The superposition of Navier's equation and the wave equation allows one to find β_A and $\beta_{(i,A)}$ in equation (20) and $\beta_{(i,B)}$ in equation (23), separately.

[22] In the upper rod, since $B \approx 0$ and $B \ll A$, the part of mode A that is related to β_A in equation (20) can be simplified to

$$u_{(u)} \approx 0, w_{(u)} \approx -Aj\frac{\omega}{c_1}\left\{\exp\left[j\omega\left(t - \frac{z}{c_1}\right)\right] - \beta_A \exp\left[j\omega\left(t + \frac{z}{c_1}\right)\right]\right\}. \tag{28a}$$

In the lower rod, with $D \approx 0$ and $D \ll C$ in equation (25):

$$u_{(l)} \approx 0,\ w_{(l)} \approx -Cj\frac{\omega}{c_1}\exp\left[j\omega\left(t - \frac{z-S}{c_1}\right)\right]. \tag{28b}$$

In the liquid, because of equations (28a) and (28b), only the plane wave is considered with $\lambda_0 = 0$ in equation (26c); thus

$$u_{(m)} = 0\ w_{(m)} = e^{j\omega\cdot t}\frac{1}{c}\left[-E_0\exp\left(-j\frac{\omega}{c}z\right) + F_0\exp\left(j\frac{\omega}{c}z\right)\right]. \tag{28c}$$

From equations (27) and (28) and considering that

$$c_1^2 = \frac{\lambda_{(u)} + 2\mu_{(u)}}{\rho_{(u)}},\quad c^2 = \frac{\lambda_{(m)}}{\rho_{(m)}},\quad Z_{(u)} = \rho_{(u)}c_1,\quad Z_{(m)} = \rho_{(m)}c,$$

four equations are obtained:

$$Z_{(u)}\frac{A\omega}{c_1}[-1 - \beta_A] = Z_{(m)}\frac{j}{c}[E_0 + F_0], \tag{29a}$$

$$-Z_{(u)}\frac{C\omega}{c_1} = Z_{(m)}\frac{j}{c}\left[E_0\exp\left(-j\frac{\omega}{c}S\right) + F_0\exp\left(j\frac{\omega}{c}S\right)\right], \tag{29b}$$

$$-Aj\frac{\omega}{c_1}(1 - \beta_A) = \frac{1}{c}(-E_0 + F_0), \tag{29c}$$

$$-j\frac{C\omega}{c_1} = \frac{1}{c}\left[-E_0\exp\left(-j\frac{\omega}{c}S\right) + F_0\exp\left(j\frac{\omega}{c}S\right)\right], \tag{29d}$$

where $Z_{(u)}$, $\rho_{(u)}$, $\lambda_{(u)}$, $\mu_{(u)}$ and $Z_{(m)}$, $\rho_{(m)}$, $\lambda_{(m)}$ are the acoustic impedances, densities, and Lame constants of the rod and liquid correspondingly. Solving equation (29) yields

$$\beta_A = \frac{1 - \exp\left(2j\frac{\omega}{c}S\right)}{\frac{Z_{(m)} - Z_{(u)}}{Z_{(m)} + Z_{(u)}} - \frac{Z_{(m)} + Z_{(u)}}{Z_{(m)} - Z_{(u)}}\exp\left(2j\frac{\omega}{c}S\right)}. \tag{30}$$

For the waves related to $\beta_{(i,A)}$ it is established that

$$\sigma_{(zz,u)} = -2\mu_{(u)}\left[\frac{B_{(i,A)}r_i}{a}\frac{j\omega_i}{c_1}J_0\left(r\frac{r_i}{a}\right)\right]\left\{\exp\left[j\omega_i\left(t - \frac{z}{c_1}\right)\right] + \beta_{(i,A)}\cdot\exp\left[j\omega_i\left(t + \frac{z}{c_1}\right)\right]\right\},$$

$$\sigma_{(zz,m)} = e^{j\omega_i t}\lambda_{(m)}\sum_{i=0}^{\infty}\left[\frac{r_n\lambda_i d_{(i,n)}}{j\omega_i a^2}\left(-E_i e^{-j\nu_i z} - F_i e^{j\nu_i z}\right) + \frac{j\nu_i^2 b_{(i,n)}}{\omega_i}\cdot(E_i e^{-j\nu_i z} + F_i e^{j\nu_i z})\right]J_0\left(\frac{r_n}{a}r\right), \tag{31}$$

$$\sigma_{(zz,l)} = -2\mu_{(u)}\left[\frac{D_{(i,A)}r_i}{a}\frac{j\omega_i}{c_1}J_0\left(r\frac{r_i}{a}\right)\right]\exp\left[j\omega_i\left(t - \frac{z-S}{c_1}\right)\right],$$

$$n = 0\ldots\infty,$$

where

$$\omega_i = \frac{c_1 r_i}{a\sqrt{(c_1/c_2)^2 - 1}}, i = 0\ldots\infty.$$

Applying the same boundary conditions of equation (27), it follows that

$$-2\mu_{(u)}\frac{B_{(i,A)}r_n}{a}\frac{j\omega_i}{c_1}\left\{1+\beta_{(i,A)}\right\}=\lambda_{(m)} \cdot\sum_{i=0}^{\infty}\left[\frac{r_n\lambda_i d_{(i,n)}}{j\omega_i a^2}(-E_i-F_i)+\frac{j\nu_i^2 b_{(i,n)}}{\omega_i}(E_i+F_i)\right] \tag{32a}$$

$$-2\mu_{(u)}\frac{D_{(i,A)}r_n}{a}\frac{j\omega_i}{c_1}=\lambda_{(m)} \cdot\sum_{i=0}^{\infty}\left[\frac{r_n\lambda_i d_{(i,n)}}{j\omega_i a^2}\left(-E_i e^{-j\nu_i S}-F_i e^{j\nu_i S}\right) +\frac{j\nu_i^2 b_{(i,n)}}{\omega_i}\left(E_i e^{-j\nu_i S}+F_i e^{j\nu_i S}\right)\right] \tag{32b}$$

$$\frac{B_{(i,A)}r_n}{a}\left\{1-\beta_{(i,A)}\right\}=\sum_{i=0}^{\infty}\frac{\nu_i b_{(i,n)}}{\omega_i}(-E_i+F_i) \tag{32c}$$

$$D_{(i,A)}\frac{r_n}{a}=\sum_{i=0}^{\infty}\frac{\nu_i b_{(i,n)}}{\omega_i}\left(-E_i e^{-j\nu_i S}+F_i e^{j\nu_i S}\right),\qquad n=0\ldots\infty. \tag{32d}$$

Equations (32) are of infinite dimension. Since $B_{(i,A)}$, $i = 1\ldots\infty$, depend on the acoustic source, they are considered to be known and $D_{(i,A)}$, E_i, F_i, $\beta_{(i,A)}$ must uniquely exist. Although the analytical solution to equation (32) is difficult to obtain, the following relation holds:

$$\beta_{(i,A)}=\beta_{(i,A)}\left(\lambda_{(m)},u_{(u)},c_1,c_2,c,a,\exp\left(2j\frac{\omega_i}{c}S\right),\exp\left(-2j\frac{\omega_i}{c}S\right)\right), \tag{33}$$

where

$$\omega_i=\frac{c_1 r_i}{a\sqrt{(c_1/c_2)^2-1}},i=0\ldots\infty.$$

Similarly, for $\beta_{(i,B)}$,

$$\beta_{(i,B)}=\beta_{(i,B)}\left(\lambda_{(m)},u_{(u)},c_2,c,a,\exp\left(2j\frac{\omega_i}{c}S\right),\exp\left(-2j\frac{\omega_i}{c}S\right)\right), \tag{34}$$

where

$$\omega_i=\frac{r_i\sqrt{2}c_2}{a},i=0,\ldots\infty.$$

[23] It is thus clear that each of the reflection coefficients, $\beta_{(i,A)}$, $\beta_{(i,B)}$, and β_A, is a periodic function of S (the thickness of the liquid), and all have the identical period

$$\Delta S=\frac{c}{2f}, \tag{35}$$

where f is the transmitted frequency from the acoustic source and c is the sound speed in the liquid. This result indicates that a change in path length S will lead to a periodic change in the echo amplitude with maxima/minima that are spaced with the same interval ΔS. Therefore, as described in the literature, the VPL method can be used to obtain c. In contrast, the FS method will not generate a periodic change in the echo amplitude except for β_A, which will be a periodic function of frequency with $\Delta f = c/2S$. Therefore the FS method is only applicable to β_A for the measurement of c.

6. Propagation of a Pulsed Wave in the RLR Model

[24] In practice, rather than a CW signal, short acoustic pulses are transmitted in the FS interferometer. The solutions for the RLR model to a pulse are obtained by superposing equation (24) over the bandwidth of the transmitted pulse. Thus, in the upper rod, with $B \ll A$ and $B \approx 0$ in equation (20), the solutions of interest are

$$u_{(p)}\approx u^f_{(p,A)}+u^b_{(p,A)}+u^f_{(p,B)}+u^b_{(p,B)} \tag{36a}$$

$$w_{(p)}\approx s\left(t-\frac{z}{c_1}\right)+h(t)*s\left(t+\frac{z}{c_1}\right)+w^f_{(p,A)}+w^b_{(p,A)} +w^f_{(p,B)}+w^b_{(p,B)}, \tag{36b}$$

where asterisk represents convolution; $h(t)$is the inverse Fourier transform [*Kovach*, 1982] of β_A, and

$$u^f_{(p,A)}(c_1t-z,r)=\sum_{i=m}^{\infty}\frac{jr_iB_{(i,A)}}{a\sqrt{(c_1/c_2)^2-1}}J_1\left(r\frac{r_i}{a}\right) \cdot\exp\left(j\frac{r_i}{a\sqrt{(c_1/c_2)^2-1}}(c_1t-z)\right),$$

$$u^b_{(p,A)}(c_1t+z,r)=\sum_{i=m}^{\infty}\frac{jr_iB_{(i,A)}}{a\sqrt{(c_1/c_2)^2-1}}J_1\left(r\frac{r_i}{a}\right)\beta_{(i,A)} \cdot\exp\left(j\frac{r_i}{a\sqrt{(c_1/c_2)^2-1}}(c_1t+z)\right),$$

$$u^f_{(p,B)}\left(\sqrt{2}c_2t-z,r\right)=\sum_{i=n}^{\infty}jB_{(i,B)}\frac{r_i}{a}J_1\left(\frac{r_i}{a}r\right) \cdot\exp\left(j\frac{r_i}{a}\left(\sqrt{2}c_2t-z\right)\right),$$

$$u^b_{(p,B)}\left(\sqrt{2}c_2t+z,r\right)=\sum_{i=n}^{\infty}jB_{(i,B)}\frac{r_i}{a}J_1\left(\frac{r_i}{a}r\right)\beta_{(i,B)} \cdot\exp\left(j\frac{r_i}{a}\left(\sqrt{2}c_2t+z\right)\right), \tag{37}$$

$$w^f_{(p,A)}(c_1t-z,r)=\sum_{i=m}^{\infty}B_{(i,A)}\frac{r_i}{a}J_0\left(r\frac{r_i}{a}\right) \cdot\exp\left(j\frac{r_i}{a\sqrt{(c_1/c_2)^2-1}}(c_1t-z)\right),$$

Table 1. Eigenfrequencies of Modes A and B With Respect to the Roots of $J_1'(r)$ for a Molybdenum Buffer Rod of 1.91 cm Diameter and Longitudinal and Shear Wave Speeds 6250 and 3350 m/s, Respectively[a]

	Index								
	0	1	2	3	4	5	6	7	8
r_i, roots	1.841	5.331	8.536	11.706	14.864	18.016	21.164	24.311	27.457
$\Delta r = r_{i+1} - r_i$	3.490	3.205	3.170	3.158	3.152	3.148	3.147	3.146	3.145
$f_i^{(A)}$, MHz	0.122	0.353	0.565	0.774	0.983	1.191	1.399	1.607	1.815
$\Delta f^{(A)} = f_{i+1}^{(A)} - f_i^{(A)}$	0.231	0.212	0.209	0.209	0.208	0.208	0.208	0.208	0.208
$f_i^{(B)}$, MHz	0.145	0.421	0.674	0.924	1.174	1.422	1.671	1.919	2.167
$\Delta f^{(B)} = f_{i+1}^{(B)} - f_i^{(B)}$	0.276	0.253	0.250	0.250	0.248	0.249	0.248	0.248	0.248

[a]The first nine roots of $J_1'(r)$ and the corresponding eigenfrequencies $f_i^{(A)}$ and $f_i^{(B)}$ are related to modes A and B, respectively. The difference between two adjacent roots is π with index number greater than 4. The difference of two adjacent eigenfrequencies of mode A is 0.208 MHz, whereas that of mode B is 0.248 MHz. The data indicate that the interfering pulses are of discrete spectrum structure.

$$w^b_{(p,A)}(c_1t+z,r) = -\sum_{i=m}^{\infty} B_{(i,A)}\frac{r_i}{a}J_0\left(r\frac{r_i}{a}\right)\beta_{(i,A)} \cdot \exp\left(j\frac{r_i}{a\sqrt{(c_1/c_2)^2-1}}(c_1t+z)\right),$$

$$w^f_{(p,B)}\left(\sqrt{2}c_2t-z,r\right) = \sum_{i=n}^{\infty} B_{(i,B)}\frac{r_i}{a}J_0\left(\frac{r_i}{a}r\right) \cdot \exp\left(j\frac{r_i}{a}\left(\sqrt{2}c_2t-z\right)\right),$$

$$w^b_{(p,B)}\left(\sqrt{2}c_2t+z,r\right) = -\sum_{i=n}^{\infty} B_{(i,B)}\frac{r_i}{a}J_0\left(\frac{r_i}{a}r\right)\beta_{(i,B)} \cdot \exp\left(j\frac{r_i}{a}\left(\sqrt{2}c_2t+z\right)\right).$$

Here the superscript f represents the forward wave, and the superscript b represents the backward wave; m and n are associated with the lowest frequencies excited within the rod and are thus determined by the lower cutoff frequency of the transmitted pulse. If the pulse covers a frequency range $[\omega_l, \infty]$, then m and n are the minimal numbers that make

$$c_1 r_m\left(a\sqrt{\left(\frac{c_1}{c_2}\right)^2-1}\right)^{-1} \geq \omega_l \quad (38)$$

$$\frac{\sqrt{2}c_2 r_n}{a} \geq \omega_l. \quad (39)$$

Since mathematically [*Bronshtein and Semendyayev*, 1998]

$$r_i \approx r_m + (i-m)\pi,\ i = m \ldots \infty,\ m \geq 5, \quad (40)$$

it follows that in equation (37), r_i can be substituted by $r_m + (i - m)\pi$ for waves of mode A and by $r_n + (i - n)\pi$ for waves of mode B, as long as ω_l or a is large enough to make $m \geq 5$ and $n \geq 5$ in equations (38)–(39).

6.1. Molybdenum Buffer Rods

[25] In most acoustic interferometry experiments applied to high-temperature silicate melts [e.g., *Katahara et al.*, 1981; *Rivers and Carmichael*, 1987; *Webb and Courtial*, 1996] the buffer rods are made of molybdenum metal, owing to its refractory and nonreactive properties. In our experimental apparatus (discussed in detail in part 2), a molybdenum upper buffer rod ($c_1 = 6250$ m/s, $c_2 = 3350$ m/s) of 1.91 cm diameter is employed. For a molybdenum rod of this dimension, the first nine roots of $J_1'(r)$ and the corresponding eigenfrequencies of mode A and mode B are given in Table 1. The entire eigenfrequencies

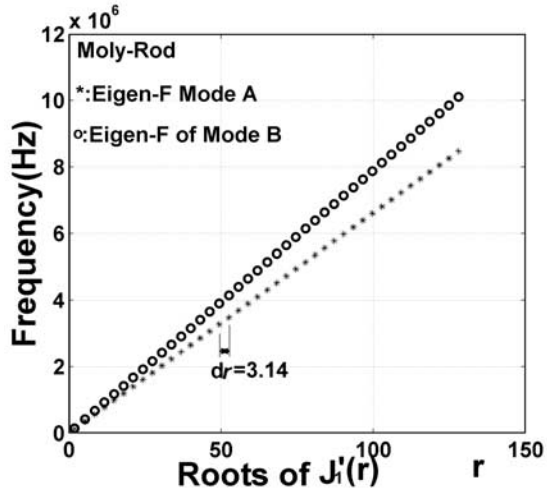

Figure 2. Set of roots of $J_1'(r)$, $r \leq 130$ for a molybdenum buffer rod of 1.91 cm diameter and longitudinal and shear wave speeds of 6250 and 3350 m/s, respectively, corresponding to eigenfrequencies of mode A from 0 to 8.6 MHz and those of mode B from 0 to 10 MHz. For index numbers greater than 4, the difference in dr between two adjacent roots is π. The difference between two adjacent eigenfrequencies of mode A is 0.208 MHz, whereas the difference between those of mode B is 0.248 MHz.

corresponding to $r_i < 130$ are plotted in Figure 2. From the former it is shown that the interfering pulses have a discrete spectrum structure. From the latter, if the employed signal frequency is greater than 2 MHz, then m and n are both greater than 8. In this case, equation (37) can be rearranged in such a way that periodic solutions are revealed:

$$\begin{aligned}
u^f_{(p,A)}(c_1t-z,r) &= \exp\left(j\frac{r_m}{a\sqrt{(c_1/c_2)^2-1}}(c_1t-z)\right)\\
&\cdot\sum_{i=m}^{\infty}\frac{jr_iB_{(i,A)}}{a\sqrt{(c_1/c_2)^2-1}}J_1\left(r\frac{r_i}{a}\right)\exp\left(j\frac{(i-m)\pi}{a\sqrt{(c_1/c_2)^2-1}}(c_1t-z)\right)\\
&= \exp\left(j\frac{r_m}{a\sqrt{(c_1/c_2)^2-1}}(c_1t-z)\right)u^f_{(A)}(c_1t-z,r)\\
&= \exp\left(j\frac{r_m}{a\sqrt{(c_1/c_2)^2-1}}(c_1t-z)\right)\\
&\cdot u^f_{(A)}\left(c_1\left(t+\frac{2a\sqrt{(c_1/c_2)^2-1}}{c_1}\right)-z,r\right)
\end{aligned}$$

$$\begin{aligned}
u^f_{(p,B)}\left(\sqrt{2}c_2t-z,r\right) &= \exp\left(j\frac{r_n}{a}\left(\sqrt{2}c_2t-z\right)\right)\\
&\cdot\sum_{i=n}^{\infty}jB_{(i,B)}\frac{r_i}{a}J_1\left(\frac{r_i}{a}r\right)\exp\left(j\frac{(i-n)\pi}{a}\left(\sqrt{2}c_2t-z\right)\right)\\
&= \exp\left(j\frac{r_n}{a}\left(\sqrt{2}c_2t-z\right)\right)u^f_{(B)}\left(\sqrt{2}c_2t-z,r\right)\\
&= \exp\left(j\frac{r_n}{a}\left(\sqrt{2}c_2t-z\right)\right)u^f_{(B)}\left(c_2\left(t+\frac{\sqrt{2}a}{c_2}\right)-z,r\right).
\end{aligned}$$

Similarly,

$$\begin{aligned}
u^b_{(p,A)} &= \exp\left(j\frac{r_m}{a\sqrt{(c_1/c_2)^2-1}}(c_1t+z)\right)u^b_{(A)},\\
u^b_{(p,B)} &= \exp\left(j\frac{r_n}{a}\left(\sqrt{2}c_2t+z\right)\right)u^b_{(B)},\\
w^f_{(p,A)} &= \exp\left(j\frac{r_m}{a\sqrt{(c_1/c_2)^2-1}}(c_1t-z)\right)w^f_{(A)},\\
w^f_{(p,B)} &= \exp\left(j\frac{r_n}{a}\left(\sqrt{2}c_2t-z\right)\right)w^f_{(B)},\\
w^b_{(p,A)} &= \exp\left(j\frac{r_m}{a\sqrt{(c_1/c_2)^2-1}}(c_1t+z)\right)w^b_{(A)},\\
w^b_{(p,B)} &= \exp\left(j\frac{r_n}{a}\left(\sqrt{2}c_2t+z\right)\right)w^b_{(B)}.
\end{aligned}\tag{41}$$

Thus the final solutions to a pulsed signal in a molybdenum upper rod are

$$\begin{aligned}
u_{(p)} &= \exp\left(j\frac{r_m}{a\sqrt{(c_1/c_2)^2-1}}(c_1t-z)\right)u^f_{(A)}(c_1t-z,r)\\
&+\exp\left(j\frac{r_m}{a\sqrt{(c_1/c_2)^2-1}}(c_1t+z)\right)u^b_{(A)}(c_1t+z,r)\\
&+\exp\left(j\frac{r_n}{a}\left(\sqrt{2}c_2t-z\right)\right)u^f_{(B)}\left(\sqrt{2}c_2t-z,r\right)\\
&+\exp\left(j\frac{r_n}{a}\left(\sqrt{2}c_2t+z\right)\right)u^b_{(B)}\left(\sqrt{2}c_2t+z,r\right)
\end{aligned}\tag{42a}$$

$$\begin{aligned}
w_{(p)} &= s\left(t-\frac{z}{c_1}\right)+h(t)*s\left(t+\frac{z}{c_1}\right)\\
&+\exp\left(j\frac{r_m}{a\sqrt{(c_1/c_2)^2-1}}(c_1t-z)\right)w^f_{(A)}(c_1t-z,r)\\
&+\exp\left(j\frac{r_m}{a\sqrt{(c_1/c_2)^2-1}}(c_1t+z)\right)w^b_{(A)}(c_1t+z,r)\\
&+\exp\left(j\frac{r_n}{a}\left(\sqrt{2}c_2t-z\right)\right)w^f_{(B)}\left(\sqrt{2}c_2t-z,r\right)\\
&+\exp\left(j\frac{r_n}{a}\left(\sqrt{2}c_2t+z\right)\right)w^b_{(B)}\left(\sqrt{2}c_2t+z,r\right).
\end{aligned}\tag{42b}$$

Here, $u^f_{(A)}$, $u^b_{(A)}$, $w^f_{(A)}$, and $w^b_{(A)}$ from mode A are four periodic pulse series with an identical time interval of $2a\sqrt{(c_1/c_2)^2-1}/c_1$. Similarly, $u^f_{(B)}$, $u^b_{(B)}$, $w^f_{(B)}$, and $w^b_{(B)}$ from mode B are four periodic pulse series with an identical time interval $\sqrt{2}a/c_2$.

[26] At this juncture, it is possible to know the format of the signal that is received by the transducer. With respect to the echo in the upper rod, for a short pulse, $s(t)$, the return signal only consists of backward waves that can be expressed as

$$\begin{aligned}
u_{(e)} &= \exp\left(j\frac{r_m}{a\sqrt{(c_1/c_2)^2-1}}(c_1t+z)\right)u^b_{(A)}(c_1t+z,r)\\
&+\exp\left(j\frac{r_n}{a}\left(\sqrt{2}c_2t+z\right)\right)u^b_{(B)}\left(\sqrt{2}c_2t+z,r\right)
\end{aligned}\tag{43a}$$

$$\begin{aligned}
w_{(e)} &= h(t)*s\left(t+\frac{z}{c_1}\right)\\
&+\exp\left(j\frac{r_m}{a\sqrt{(c_1/c_2)^2-1}}(c_1t+z)\right)w^b_{(A)}(c_1t+z,r)\\
&+\exp\left(j\frac{r_n}{a}\left(\sqrt{2}c_2t+z\right)\right)w^b_{(B)}\left(\sqrt{2}c_2t+z,r\right).
\end{aligned}\tag{43b}$$

Since β_A changes periodically with a frequency interval of $\Delta f = c/2S$ in equation (30), the frequency response function of $h(t)$ must have maxima/minima at the same frequency interval. If the positions of these maxima/minima can be determined, then the sound speed in the liquid (c) can be inferred from them. For $h(t)$, since the reflection coefficient

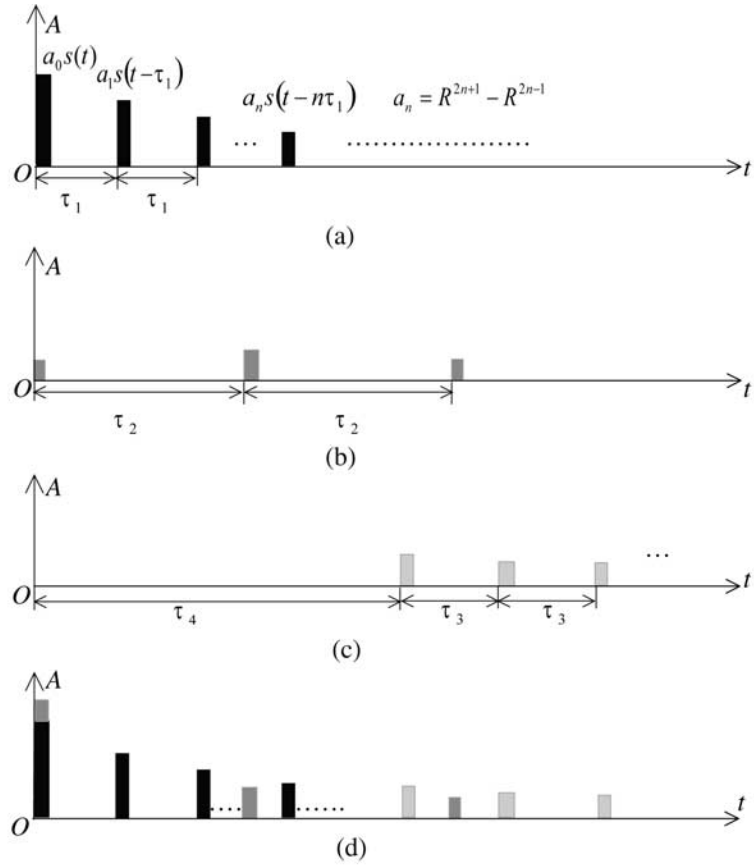

Figure 3. Visual summary of the format and pattern of the entire received longitudinal wave $w_{(e)}$. (a) Mirror reflections with periodic pulse interval $\tau_1 = 2Sc^{-1}$, velocity c_1 and reflection coefficients $a_0 = R$, $a_n = R^{2n+1} - R^{2n-1}$, $n = 1 \ldots \infty$. (b) Interfering pulses of mode A, $\exp\{j[r_m/a\sqrt{(c_1/c_2)^2-1}](c_1 t + z)\} w^b_{(A)}$, with periodic pulse interval $\tau_2 = 2ac_1^{-1}\sqrt{(c_1/c_2)^2-1}$ and velocity c_1. (c) Interfering pulses of mode B, $\exp\{j(r_n/a)(\sqrt{2}c_2 t + z)\} w^b_{(B)}$, with periodic pulse interval $\tau_3 = \sqrt{2}ac_2^{-1}$, relative arrival time delay $\tau_4 = 2L|c_1^{-1} - (\sqrt{2}c_2)^{-1}|$ (compared to the arrival of the first mirror reflection wave) and velocity $\sqrt{2}c_2$. (d) Entire echo (longitudinal part) $w_{(e)}$, the sum of all the waves in Figures 3a–3c.

can be expanded to

$$\beta_A = R\left[1 - \exp\left(-2j\frac{\omega}{c}S\right)\right]\sum_{n=0}^{\infty}\left[R^2\exp\left(-2j\frac{\omega}{c}S\right)\right]^n = R + R\sum_{n=1}^{\infty}\left(R^{2n} - R^{2n-2}\right)\left[e^{-2j\frac{\omega}{c}S}\right]^n \tag{44a}$$

by the inverse Fourier transform of β_A,

$$h(t) = F^{-1}(\beta_A) = R\delta(t) + \sum_{n=1}^{\infty}\left(R^{2n+1} - R^{2n-1}\right)\delta\left(t - \frac{2nS}{c}\right), \tag{44b}$$

it follows that

$$E(t) = h(t) * s(t) = Rs(t) + \sum_{n=1}^{\infty}\left(R^{2n+1} - R^{2n-1}\right)s\left(t - \frac{2nS}{c}\right), \tag{45}$$

In equations (44a), (44b), and (45),

$$R = \frac{Z_{(m)} - Z_{(u)}}{Z_{(m)} + Z_{(u)}}$$

and $\delta(t)$ is the impulse function.

[27] Physically, the right-hand side of equation (45) represents a series of mirror reflections of the transmitted pulse with a time gap of $2S/c$ between two adjacent reflections. This time gap is the critical feature of the frequency-sweep interferometer; it provides the foundation for a signal-processing algorithm from which c can be deduced from spectrum analysis (part 2).

[28] For the rest of the received signal, $w_{(e)}$, parts

$$\exp\left\{j\left[\frac{r_m}{a\sqrt{(c_1/c_2)^2-1}}\right](c_1 t + z)\right\} w^b_{(A)}(c_1 t + z, r)$$

and $\exp[j(r_n/a)](\sqrt{2}c_2 t + z)\, w^b_{(B)}(\sqrt{2}c_2 t + z, r)$ are interfering pulses that are expected to be observed in experiments. Since $w^b_{(A)}$ and $w^b_{(B)}$ are two series of periodic pulses that

Table 2. Material Parameters

Material	c_1, m/s	c_2, m/s	P Wave Impedance, kg/m^2 s $\times$ 10^6
Aluminum	6320	3130	17.06
Molybdenum	6250	3350	63.75
Air	340	NA[a]	0.413

[a]NA, not available.

are modulated by different sinusoid waves as shown in equation (42), the interfering signal is the addition of two pulse series, one with time interval $2a\sqrt{(c_1/c_2)^2-1}/c_1$ and group velocity c_1, the other with time interval $\sqrt{2}a/c_2$ and group velocity $\sqrt{2}c_2$. The same conclusion is also applicable to $\exp\left[j\left(r_m/a\sqrt{(c_1/c_2)^2-1}\right)(c_1t+z)\right]u^b_{(A)}$ and $\exp\left[j(r_n/a)\left(\sqrt{2}c_2t+z\right)\right]u^b_{(B)}$.

6.2. Visual Summary

[29] The results of the above discussion are illustrated in Figures 3a–3d, where the received signal $w_{(e)}$ in Figure 3d is the sum of those in Figures 3a–3c; $u_{(e)}$ is neglected in this study because of the very narrow beam angle of the transducer about the z axis (a longitudinal transducer was employed in the following experiments). In Figure 3a the mirror reflections of the transmitted pulse contribute most of the acoustic energy to the echo signal, which is the case for rods made of molybdenum metal. In the first arrival the ratio of the amplitude of the mirror reflection to that of the interfering pulse in Figure 3b may be up to 20–30 dB, which is large enough to allow the first interfering pulse to be neglected in signal processing.

[30] The time interval $\tau_1$between two adjacent reflections is related to the path length (S) and the sound speed of the liquid (c). Mirror reflections travel with speed c in the liquid and have the same waveform except for the first arrival, which has an opposite polarization to those of the rest. In Figures 3b and 3c, however, the pulses are not reflections of the transmitted signal but are interfering waves that are determined by the diameter and material of the rod and the transmitted pulse itself. Importantly, the time intervals between the adjacent two pulses in both Figures 3b and 3c are dependent only on the material and diameter of the rod and have nothing to do with the transmitted waveform or the employed frequency. One can benefit from this result by choosing a suitable material and diameter for the rod in order to adjust the time intervals and thus separate the mirror reflection from those of the interfering pulses. In addition, because the pulses of mode B in Figure 3c have a smaller group speed than those in Figures 3a and 3b and are far behind the mirror reflections by τ_4, where L is the length of the upper rod, they are easily removed from the echo, which enhances signal processing.

[31] It can also be seen in Figure 3 that the acoustic ray model only deals with mirror reflections and thus cannot explain the interfering portion of the signal. From this viewpoint, the ray model is only an approximation of equation (43), which is the entire received signal. For the VPL method the ray model approximation makes no difference for the measurement of liquid sound speed (c) because the amplitude of the interfering signal obeys the same periodical change with path length S, as do the mirror reflections. However, this is not the case for the FS method unless the interfering pulses can be removed from the echo so that the mirror reflection signal can be obtained. Fortunately, it is feasible to achieve this through system design, which is treated and demonstrated by experimental examination in part 2 of this series of papers. Although the interfering pulses of modes A and B can be removed from the echo by system design, it is nonetheless important to understand the physical interpretation of these waves, which is discussed in Appendix A.

7. Experimental Test of the Acoustic Model

[32] In order to test the conclusions drawn above from our theoretical analysis of the general acoustic model and the

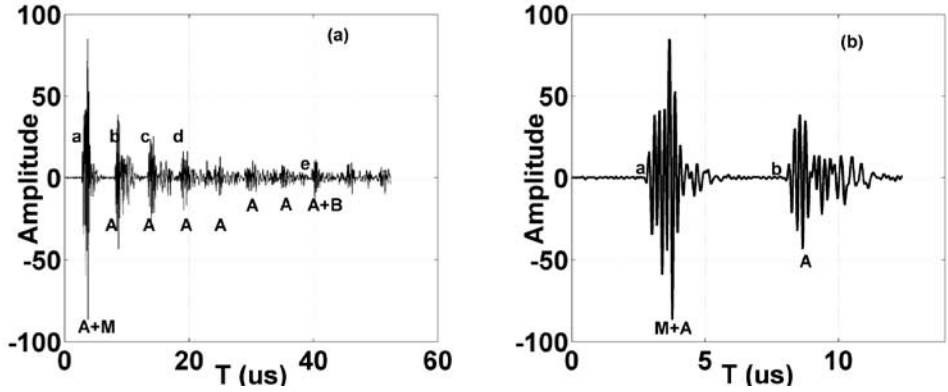

Figure 4. Experimental results from the aluminum rod (25 cm long) in air at room temperature. (a) Entire echo, which is a series of pulses. The first pulse consists of the first mirror reflection (M) and the first interfering pulse of mode A (A). The rest are interfering pulses of mode A. After time e, pulses of mode B arrive and are merged with pulses of mode A. The times at a, b, c, d, e are 2.60, 8.00, 13.40, 18.80, 36.60 μs, respectively. The times do not reflect the arrival time delay relative to the trigger pulse and thus only have relative meaning. (b) Magnification of the first part of the echo in Figure 4a, where the first (and only) mirror reflection (M) and the first and second interfering pulses of mode A are shown. See text for discussion.

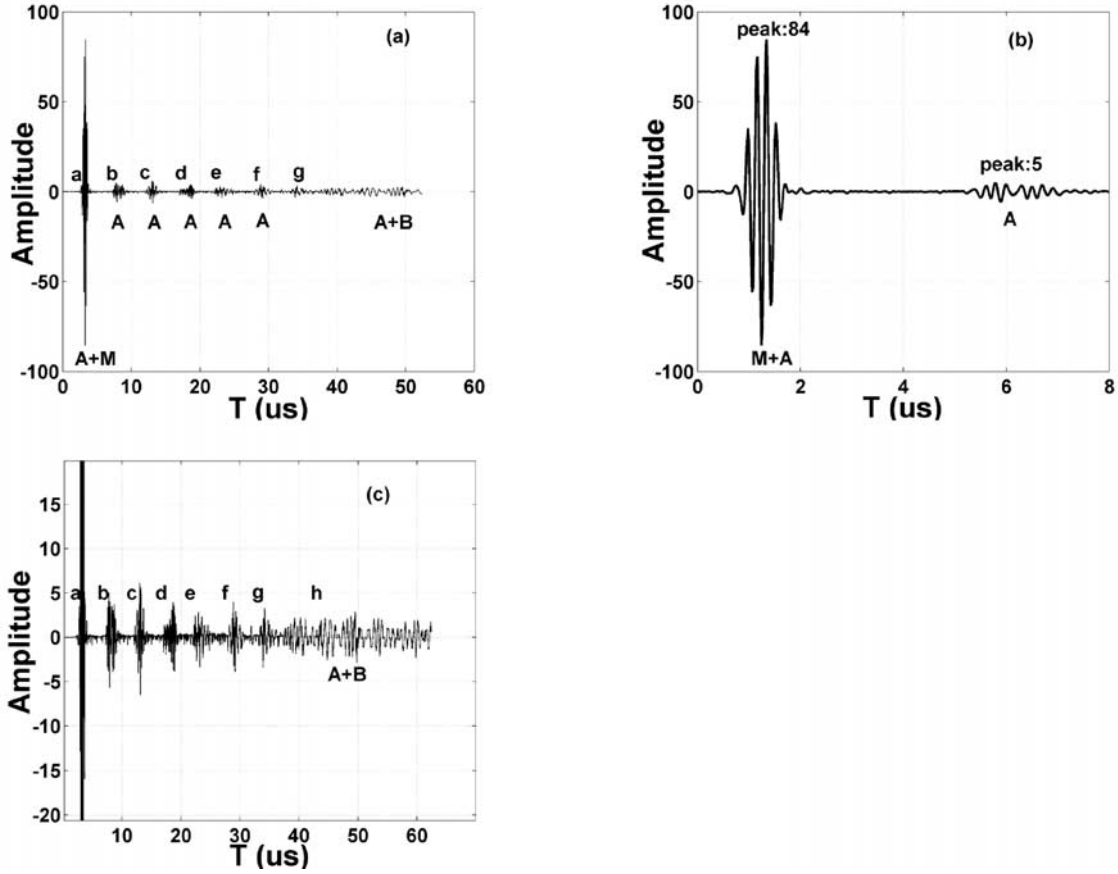

Figure 5. Experimental results from the molybdenum rod (40 cm long) in air at room temperature. (a) Entire echo, which is a series of pulses. The first pulse consists of the first mirror reflection (M) and the first interfering pulse of mode A (A). The rest are interfering pulses of mode A. The times at a, b, c, d, e, f, g are 2.54, 7.20, 11.96, 16.84, 21.80, 27.60, 32.50 μs, respectively. The times do not reflect the arrival time delay relative to the trigger pulse and thus only have relative meaning. (b) Horizontally enlarged version of the first part of the echo in Figure 5a, where the first (and only) mirror reflection and the first and second interfering pulses of mode A are shown. The time axis is a window extracted from that in Figure 5a; thus the timescale only has relative meaning. In contrast to Figure 4b, the amplitude of the interfering pulses is significantly smaller than that of the mirror reflection, owing to the higher acoustic impedance of molybdenum versus aluminum metal. (c) Vertically enlarged version of Figure 5a. After time h, pulses of mode B arrive and are merged with pulses of mode A. The first pulse of mode B arrives at h = 42.54 μs. Compared to the first mirror reflection, it is delayed by (42.54−2.54) = ∼40 μs.

resultant wave equations, experiments were conducted on both aluminum and molybdenum buffer rods at room temperature, with air substituting for liquid in the RLR model, and on a molybdenum rod in a silicate liquid at 1436°C. The longitudinal (dilatational) and transversal (rotational) sound velocities in aluminum, molybdenum, and air are listed in Table 2 along with their acoustic impedances.

7.1. Aluminum Buffer Rod in Air

[33] A 5 MHz 5cycle long CW pulse (1 μs duration) was sent down an aluminum rod (c_1= 6320 m/s, c_2 = 3130 m/s) of 1.906 cm diameter and 25 cm length. The echo was collected at a 50 MHz sample rate and is shown in Figure 4. Owing to the severely unmatched impedances between air and metal, no mirror reflections other than the first were observed in these experiments. This is an ideal configuration for isolating the features in the echo train associated with wave propagation in the buffer rod only. In Figure 4a the entire echo is shown and is a series of pulses. Figure 4b is a magnification of the first part of the echo in Figure 4a, where the first (and only) mirror reflection and the first and second interfering pulses of mode A are shown; note that the first interfering pulse is merged with the first mirror reflection. The spreading tail portion of the first pulse in Figure 4b suggests that this pulse is not entirely composed of the single frequency that was transmitted and is likely corrupted by an interfering portion, which is undoubtedly the first interfering pulse of mode A. The second pulse in Figure 4b is the second interfering pulse of mode A, which has a totally different waveform from that of the first pulse and is thus not the reflection of the first pulse.

[34] In Figure 4a the relative arrival times of the mirror reflection and the interfering pulses of mode A are roughly estimated and marked by *a*, *b*, *c*, and *d*, respectively, from which one can estimate the time delays between adjacent

pulses. For example, the first two pulses are separated by the distance between *a* and *b*, which is equal to ~5.4 μs. This result is in good agreement with the time delay derived from the theoretical model in Figure 2. In the theoretical case, the time delay is $\tau_2 = 5.29$ μs.

[35] To gain further insight into the nature of the pulses illustrated in Figure 4, a second experiment was performed to test whether the time gaps between adjacent pulses were dependent on the length of the buffer rod. In this second experiment the aluminum rod was 70 cm length (and the same diameter), and the first four pulses in the echo showed almost the same time gaps as those in Figure 4a. This result verifies that the interfering pulses of mode A are traveling at the same group velocities (otherwise, the time delays should increase with rod length), which in turn indicates that they are not waves of different modes. From the length of the rod and the measurement of the time delay between the transmitted signal and the first returning pulse, the wave speed of the first pulse was determined; it is identical to the speed of the longitudinal wave, 6320 m/s. Thus it is further concluded that the interfering pulses of mode A have the same group velocity as that of the longitudinal wave, which is predicted from the theoretical model discussed above. With respect to the interfering pulses of mode B, it is hard to distinguish them in Figure 4a from those of mode A. However, from the acoustic model one can estimate their delay time $\tau_4 = 34$ μs, which places their arrival at time *e* in Figure 4a.

[36] A key point to emphasize is that the above experimental observations could not be completely explained by the solutions of the accurate wave equation without the derivations in equations (14)–(19), where the boundary conditions were set to be close to but not identical to zero. It was the adoption of these boundary conditions that avoided the mathematical difficulties in finding the wave solutions and, most importantly, introduced the interfering pulses of mode A, which reasonably represent the propagation phenomena observed in experiments described above. This conclusion is made stronger by the experimental results on the molybdenum rod, discussed below.

7.2. Molybdenum Buffer Rod in Air

[37] For the experiment on the molybdenum rod (c_1 = 6250 m/s, c_2 = 3350 m/s) in air at 20°C, the transmitted pulse was adjusted to a 5.8 MHz 5 cycle CW signal (0.862 μs duration). The rod was 1.910 cm diameter and 40 cm length. The entire echo is shown in Figure 5a, and the magnification of its first two pulses is shown in Figure 5b. A significant difference between Figures 4 and 5 (aluminum versus molybdenum rods) is that the amplitudes of the interfering pulses of mode A drop dramatically in Figure 5 (the molybdenum rod) compared with the amplitude of the first (and only) mirror reflection. Generally speaking, this is because molybdenum is much denser than aluminum and thus has a larger acoustic impedance; therefore more acoustic energy is confined and reflected in the molybdenum rod. As such, the first mirror reflection in Figure 5 is stronger. As shown in Figure 5b, the peak value 84 of the first pulse is 25 dB higher than that of the second interfering pulse. If the first interfering pulse has the same peak value as the second interfering pulse, then such a big difference in the amplitude between the mirror reflection (large) and the first interfering pulse (small) allows the first pulse to be considered a pure mirror reflection. This conclusion is supported by the observation that the first arrival in Figure 5b is very close to a 5.8 MHz CW pulse. In addition, because its velocity was measured and found to be identical to that of the longitudinal wave, one can conclude that it is a nondispersive wave, which supports the existence of the plane wave derived in the model.

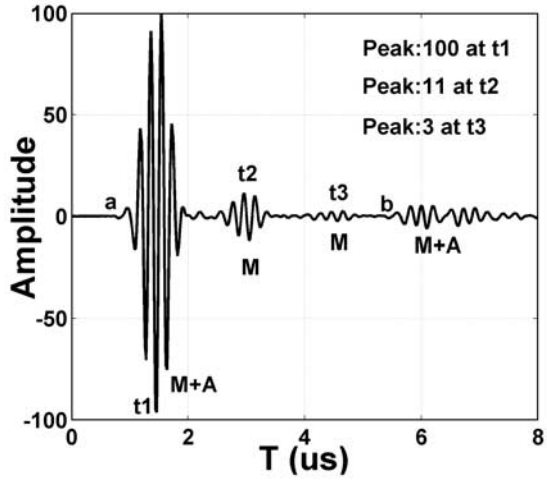

Figure 6. Experimental result from the molybdenum rod (40 cm long) in contact with a silicate melt (NAS-8) at 1436°C. Three mirror reflections are well resolved in the return signal before the second interfering pulse of mode A. The time delay between the first two mirror reflections is measured by $t_2 - t_1 = 2.98 - 1.48 = 1.5$ μs ($t_3 = 4.48$ μs, a = 0.60 μs, b = 5.40 μs). The phase of the first mirror reflection is different from those of the rest by 180°.

[38] Moreover, both the format and pattern of the experimentally observed echo within the molybdenum rod are fully consistent with that predicted from the model. For example, from the experimental data in Figures 5a and 5c the delay between the first two pulses is approximately, τ_2 = 7.20 – 2.54 = 4.66 μs, whereas the delay time calculated from the theoretical model is $\tau_2 = 4.81$ μs. Similarly, the arrival time of the first interfering pulse of mode B is estimated from the experimental graph in Figure 5c to be at position $h = 42.54$ μs, such that $\tau_4 = 42.54 - 2.54 = 40$ μs. This experimentally observed time delay is in agreement with that derived from the theoretical acoustic model, τ_4 = 40 μs.

7.3. Molybdenum Rod in Silicate Liquid at High Temperature

[39] In this final experiment the same molybdenum rod as used in air was placed in contact with a silicate melt (sample NAS-8 from *Kress et al.* [1988]) at 1436°C in a reducing atmosphere (99% Ar, 1% CO). The same 5.8 MHz 5 cycle CW signal was transmitted down the rod. Because the acoustic impedances between silicate liquid and metal are not as severely unmatched as those between air and metal, three mirror reflections are observed in the return signal before the second interfering pulse of mode A; these reflections have peak values of 100, 11, and 3, respectively (Figure 6). The second and third reflections differ in phase

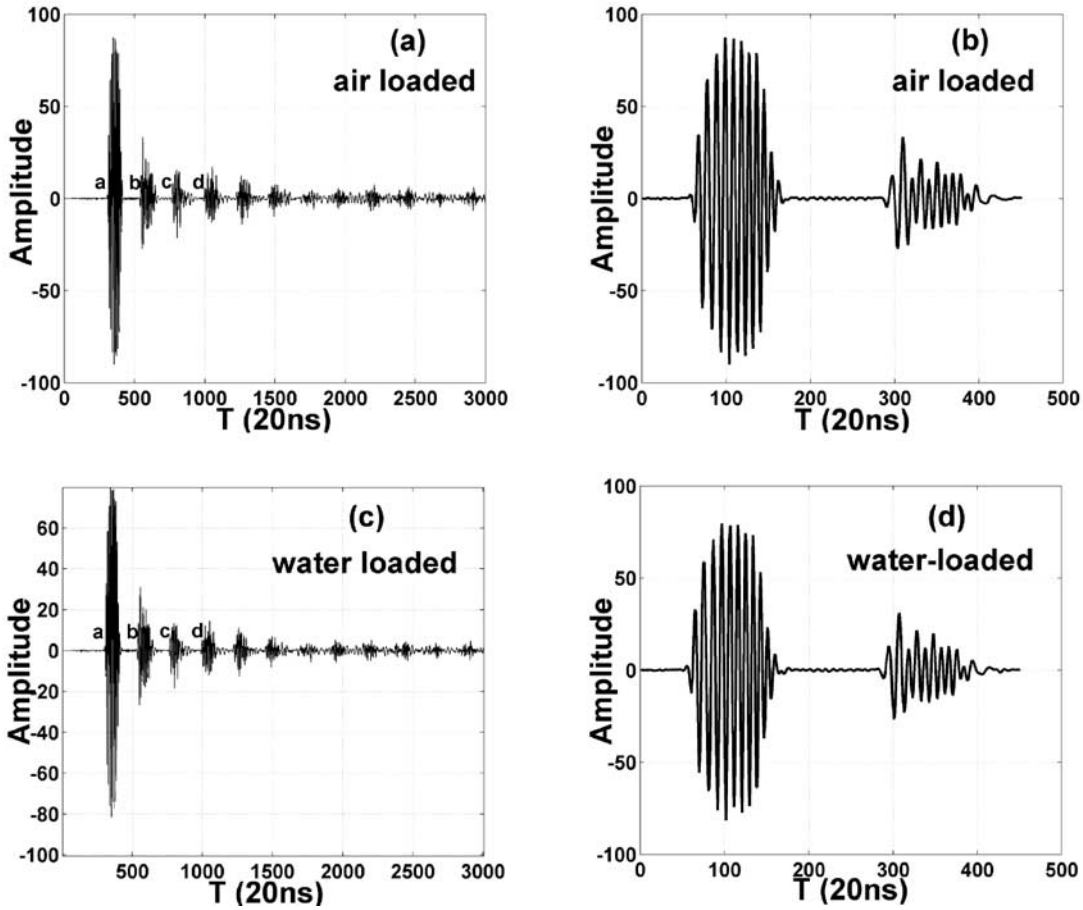

Figure 7. Echo signal from a FM pulse with duration 2 μs and frequency range from 4 to 6 MHz. (a) Echo from an air-loaded molybdenum rod. (b) Horizontally enlarged version of the first two pulses in Figure 7a. (c) Echo from a water-loaded molybdenum rod. (d) Horizontally enlarged version of the first two pulses in Figure 7c.

from the first by 180°; their waveforms are the upside down version of the first. The results in Figure 6 illustrate two critical points. First, they show that the use of a molybdenum buffer rod with a diameter $\geq$1.9 cm is ideal for application of the FS method to the measurement of silicate melt sound speeds, owing to the excellent resolution of three mirror reflections before an interfering pulse is observed. Second, because this experiment was performed at a temperature more than 1400° higher than that performed in air, it allows a test of whether the delay time between interfering pulses of mode A is dependent on temperature. The echo shown in Figure 6 indicates a delay time between the first two interfering pulses of $\tau_2 = 5.40 - 0.60 = 4.80$ μs, which is nearly identical to the theoretical value (4.81 μs) calculated above. Therefore the period of the interfering series of mode A is independent of temperature within experimental resolution.

7.4. Pressure Dependence of the Echo Format and Pattern in the Upper Rod

[40] A primary motivation for the development of FS interferometry is to extend relaxed sound speed measurements on silicate liquids to high pressure in an internally heated pressure vessel (IHPV). In the theoretical acoustic model presented above, nearly stress-free boundary conditions were applied to the cylindrical surfaces of the buffer rods. This is an excellent approximation for the interface between the molybdenum rods and the gas at 1 bar owing to the poorly matched acoustic impedances between the rod and the enclosing gas (99% Ar, 1% CO). Additionally, since the circumference area of the upper rod immersed in the melt is only a small fraction of the entire rod length, no significant differences are observed between an echo from a rod completely enclosed in gas and that from a rod partially immersed (2–3 mm) into the melt. However, the high density of the gas medium in an IHPV at high pressure may lead to acoustic energy coupling between the buffer rods and gas.

[41] An experimental evaluation of this effect is presented in Figure 7 by comparing the waveforms of echo signals obtained in two experiments where a molybdenum rod (1.91 cm diameter and 40 cm length) was immersed in air versus liquid water at 1 bar and room temperature. Liquid water at these conditions mimics the conditions of immersing a rod in a high-density gas in an IHPV. The echoes of a frequency modulated (FM) chirp pulse, with

Table 3. Comparison of Air-Loaded Versus Water-Loaded Cases

Data Segment (From Point to Point)	Correlation Coefficient
1–500	0.9972
1–1000	0.9937
1–1500	0.9919
1–2000	0.9909
1–2500	0.9892
1–3000	0.9879
500–1500	0.9515
1000–2000	0.9263
1500–2500	0.8165
2000–3000	0.7407

2 μs duration and a frequency range of 4–6 MHz, in both air-loaded and water-loaded cases, were sampled at 50 MHz and are shown in Figures 7a and 7c, respectively. The relative starting positions of the first four pulses in each echo are marked by *a*, *b*, *c*, *d*, which are marked as 300, 533, 766, 999 on the 20 ns scale; they correlate to 6, 10.66, 15.32, and 19.98 μs, respectively. These data show that the relative positions of the first four pulses do not vary with the density of the medium surrounding the rod. In addition, the waveform of the entire echo is very similar. Table 3 shows the correlation coefficients between corresponding segments of the two waveforms extracted from Figures 7a and 7c. For the segment between points 1 and 500, which contains the first pulse, the correlation coefficient is 0.9972. This illustrates that the first pulse in Figure 7a and the first pulse in Figure 7c are almost identical and differ only in amplitude. Figures 7b and 7d show enlarged versions of the first pulse in the air-loaded and water-loaded cases, respectively. With the increase of the length of the examined echo segment the correlation coefficient drops to 0.9879. However, the major part of the entire waveform in Figure 7a is well correlated with and almost identical to that in Figure 7c.

[42] To gain further insight into the correlation of the interfering pulses of modes A and B, signal segments between 500 and 3000 were examined. The correlation coefficients between these segments are shown in Table 3. With a window width of 1000 points the coefficient changes from 0.9515 to 0.7407 as the window shifts from left to right. This indicates that the interfering pulses of mode A, which arrive first, are almost independent of the density of the medium surrounding the rod, whereas with the arrival of the pulses from mode B, the combined signals of modes A and B are dependent on the density of the surrounding medium. However, this dependence does not make any difference in the performance of the FS interferometer because the echo is truncated and the interfering pulses are not used for signal processing (see part 2).

[43] In summary, for the portion of the signal that is used for FS interferometry the two waveforms in Figures 7a and 7c are nearly identical with a correlation coefficient of 0.9972. This result strongly indicates that the basic format and pattern of the echo segment used to obtain sound speed by the FS method will not be altered by immersion of the interferometer in a gas medium at high pressure. In the meantime, we have completed a full theoretical analysis of acoustic propagation in a gas-loaded rod according to the accurate elastic wave equation that confirms these experimental results; it will be presented in a future contribution.

8. Conclusions

[44] A general acoustic model of the RLR interferometer and solutions to the resultant wave equations are presented and confirmed by experiment. The model is successful in explaining the mirror reflections and the interfering pulses observed in experiments of the interferometer system. From the solutions the format of the echo signal is precisely quantified. According to the model a series of plane waves (mirror reflections from the liquid) and two series of interfering pulses (modes A and B) exist in the return signal, in which pulses of mode A and the plane waves have the same group velocity, whereas pulses of mode B travel at a slower speed. Both mode A and mode B waves are nondispersive. The first return pulse consists of both the plane wave and the first pulse of mode A, and thus it is not exactly a mirror copy of the transmitted wave. However, the amplitude of the interfering portion from mode A is much smaller than that of the mirror reflection when a suitable buffer rod material is selected (e.g., a molybdenum buffer rod), and thus it can be neglected. Experiments on molybdenum and aluminum rods with different dimensions provide data that confirm the acoustic model. The results indicate that a molybdenum buffer rod of $\geq$1.9 cm diameter is effective for the measurement of relaxed sound speeds in silicate melts with a frequency sweep interferometer. In addition to guiding the choice of rod material and dimensions the theoretical model further guides the format design of the transmitted pulse and implementation of the signal-processing algorithm, all of which are discussed and described in part 2 of this series of papers, where the successful application of frequency sweep interferometry to high-temperature silicate liquids is demonstrated.

Appendix A: Physical Interpretation of Waves of Modes A and B

[45] Although the interfering pulses of modes A and B can be removed from the echo through system design, it is nonetheless important to understand the physical interpretation of these waves. The mirror reflections used to measure liquid sound speed are longitudinal waves identical to those interpreted by the simplified acoustic ray model [*Katahara et al.*, 1981; *Rivers*, 1985]. The reflection coefficients in equations (30) and (45) are the same as those presented in the same reference above. In contrast, the interfering waves of both modes A and B are composed of both longitudinal (w) and shear (u) components, the latter of which accounts for the necessary radial variation in displacement in order for the former to propagate down and up the rod. These waves result from the interaction of vibration with the circumferential boundary of the rod; they are characterized by a series of eigenfrequencies that are independent of the excitation but instead are determined by the dimension and material of the rod.

[46] An example of some radial variations of the particle displacement associated with some representative eigenfrequencies is given in Figure A1 for both modes, where the

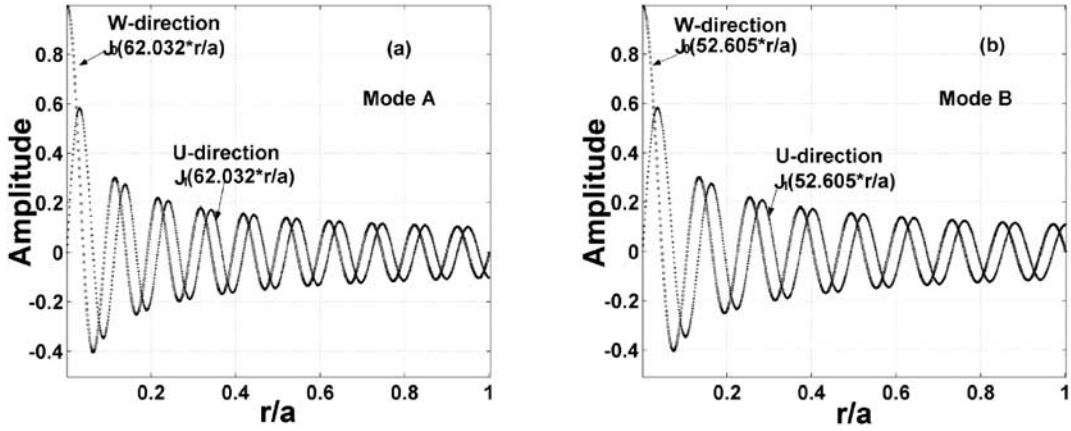

Figure A1. Radial variation of particle displacements of both longitudinal (w) and shear (u) components. For a transmitted pulse of 4–6 MHz, eigenfrequencies 4.1023 MHz of mode A and 4.1530 MHz of mode B will be excited within a molybdenum buffer rod of 1.91 cm diameter, corresponding to two roots of $J_1'(r)$, $r_m = 62.032$, and $r_n = 52.602$ associated with root index numbers 19 and 16, respectively, in Figure 2, according to equations (19), (22), (38), and (39). (a) Radial variation of particle displacement of longitudinal part (w) J_0 (62.032(r/a)) and that of shear part (u) J_1 (62.032(r/a)) of mode A. (b) Radial variation of particle displacement of longitudinal part (w) J_0 (52.605(r/a)) and that of shear part (u) J_1 (52.605(r/a)) of mode B.

lower cutoff frequency of the incident signal is 4 MHz. In this case, the lowest eigenfrequency of mode A is 4.1023 MHz, while that of mode B is 4.1530 MHz, with respect to root index numbers 19 and 16, respectively, in Figure 2 for a 1.91 cm diameter molybdenum buffer rod. In general, a subset of all the eigenfrequencies will be excited by the incident wave and will always constitute two kinds of pulse chains (modes A and B) with both longitudinal and shear components in each kind. In mode A both the longitudinal and shear waves contain the same eigenfrequencies, have the identical pulse interval $2a\sqrt{(c_1/c_2)^2-1}/c_1$, and are modulated by the smallest eigenfrequency $c_1 r_m (a\sqrt{(c_1/c_2)^2-1})^{-1}$ that is greater than or equal to the lower cutoff frequency, ω_l, of the excitation. Similarly in mode B, the interval and modulation frequency are $\sqrt{2}a/c_2$ and $\sqrt{2}c_2 r_n/a$, respectively. Here m and n are the index numbers of roots of $J'(x)$, corresponding to the two modulation frequencies.

[47] The major difference between modes A and B, except for the waveforms and frequency compositions, is that they travel at different speeds, c_1 and $\sqrt{2}c_2$, respectively. Since both the longitudinal and shear waves of the same mode have the same speed, it is possible that the shear waves can be detected at the arrival time of the associated longitudinal waves. It is interesting to observe from experiment (not presented in this paper) that when a 5 MHz 5 cycle CW pulse is sent down a molybdenum rod of length L though a shear wave transducer, the first return (an interfering shear wave pulse of mode A without the longitudinal mirror reflection included) is received by the same transducer right after a time delay of $2L/c_1$, and the whole shear wave chain has the same format as that of the interfering longitudinal wave chain.

[48] The detection of waves of mode B (both longitudinal and shear components) is more difficult because they are merged with those of mode A in the case of pulse excitation. One way to detect them, however, is to transmit a long CW pulse at a frequency close to an eigenfrequency of mode B but different from any of mode A so that the energy of mode B will be relatively enhanced. Another method for detection of mode B waves is to adjust (if possible) the diameter of the rod to gain ideal eigenfrequency distributions of both modes A and B in order that the response of mode B can be enhanced at certain frequencies for its detection through signal processing, like a Notch filter. In conducting experiments to detect waves of mode B, use of a shear wave transducer is recommended because of better detection when mirror reflections are eliminated.

[49] **Acknowledgments.** This research was supported by the National Science Foundation (EAR-0087764). In addition, both the Department of Geological Sciences and the College of Literature, Science and Art at the University of Michigan provided seed funds for this research. Constructive comments from Ian Carmichael, Ian Jackson, Mark Rivers, and an anonymous reviewer substantially improved the manuscript.

References

Achenbach, J. D. (1973), *Wave Propagation in Elastic Solids*, 425 pp., North-Holland, New York.

Agee, C. B., and D. Walker (1993), Olivine flotation in mantle melt, *Earth Planet. Sci. Lett.*, *114*, 315–324.

Ai, Y., and R. Lange (2004), An ultrasonic frequency sweep interferometer for liquids at high temperature: 2. Mechanical assembly, signal processing, and application, *J. Geophys. Res.*, B12204, doi:10.1029/2004JB003062.

Aris, R. (1962), *Vectors, Tensors and the Basic Equations of Fluid Mechanics*, 286 pp., Dover, Mineola, N. Y.

Billingham, J., and A. C. King (2000), *Wave Motion*, 468 pp., Cambridge Univ. Press, New York.

Bronshtein, I. N., and K. A. Semendyayev (1998), *Handbook of Mathematics*, 973 pp., Springer-Verlag, New York.

Chen, G. Q., T. J. Ahrens, and E. M. Stolper (2002), Shock wave equation of state of molten and solid fayalite, *Phys. Earth Planet. Inter.*, *134*, 35–52.

Chou, P. C. (1992), *Elasticity Tensor, Dyadic, and Engineer Approaches*, 290 pp., Dover, Mineola, N. Y.

Davies, R. M. (1948), A critical study of the Hopkinson pressure bar, *Philos. Trans. R. Soc. London, Ser. A*, *240*, 375–457.
Farlow, S. J. (1993), *Partial Differential Equations for Scientists and Engineers*, 414 pp., Dover, Mineola, N. Y.
Graff, K. F. (1975), *Wave Motion In Elastic Solids*, 649 pp., Dover, Mineola, N. Y.
Katahara, K. W., C. S. Rai, M. H. Manghnani, and J. Balogh (1981), An interferometric technique for measuring velocity and attenuation in molten rocks, *J. Geophys. Res.*, *86*, 11,779–11,786.
Kress, V. C., Q. Williams, and I. S. E. Carmichael (1988), Ultrasonic investigation of melts in the system Na_2O-Al_2O_3-SiO_2, *Geochim. Cosmochim. Acta*, *52*, 283–293.
Kingsler, L. E. (2000), *Fundamentals of Acoustics*, 548 pp., John Wiley, Hoboken, N. J.
Kovach, L. D. (1982), *Advanced Engineering Mathematics*, 706 pp., Addision-Wesley-Longman, Reading, Mass.
Li, B., I. Jackson, T. Gasparik, and R. C. Liebermann (1996), Elastic wave velocity measurement in multi-anvil apparatus to 10 GPa using ultrasonic interferometry, *Phys. Earth Planet. Inter.*, *98*, 79–91.
Li B., G. Chen , D. G. Gwanmesia , and R. C. Liebermann (1998), Sound velocity measurement at mantle transition zone conditions of pressure and temperature using ultrasonic interferometery in a multianvil apparatus, in *Properties of Earth and Planetary Materials at High Pressure and Temperature*, *Geophys. Monogr. Ser.*, vol. 101, edited by M. H. Manghnani and T. Yagi, pp. 41–61, AGU, Washington, D. C.
Mason W. P. (1958), *Physical Acoustics and the Properties of Solids*, 402 pp., Van Nostrand Reinhold, Hoboken, N. J.
Mason, W. P. (1965), *Physical Acoustics- Principles and Methods*, vol. 1 (A), 476 pp., Academic, San Diego, Calif.
Nagy, P. B. (1995), Longitudinal guided wave propagation in a transversely isotropic rod immersed in fluid, *J. Acoust. Soc. Am.*, *98*, 454–457.
Rivers M. L. (1985), Ultrasonic studies of silicate melts. Ph. D. thesis, Univ. of Calif., Berkeley.
Rivers M. L., and I. S. E. Carmichael (1987), Ultrasonic studies of silicate melts, *J. Geophys. Res.*, *92*, 9247–9270.
Secco, R. A., M. H. Manghnani, and T. C. Liu (1991), Velocities and compressibility of komatiitic melts, *Geophys. Res. Lett.*, *18*, 1397–1400.
Shen A. H., H.-J. Reichmann, G. Chen, R. J. Angel, W. A. Bassett, and H. Spetzler (1998), GHz ultrasonic interferometry in a diamond anvil cell: P-wave velocity in periclase to 4. 4 GPa and 207°C, in *Properties of Earth and Planetary Materials at High Pressure and Temperature*, *Geophys. Monogr. Ser.*, vol. 101, edited by M. H. Manghnani, pp. 71–77, AGU, Washington, D. C.
Soutas-Little, R. W. (1999), *Elasticity*, 431 pp., Dover, Mineola, N. Y.
Thurston, R. N. (1978), Elastic waves in rods and clad rods, *J. Acoust. Soc. Am.*, *64*, 1–37.
Webb, S. L., and P. Courtial (1996), Compressibility of melts in the CaO-Al_2O_3-SiO_2 system, *Geochim. Cosmochim. Acta*, *60*, 75–86.

Y. Ai and R. Lange, Department of Geological Sciences, 2534 C.C. Little Building, University of Michigan, Ann Arbor, MI 48109-1063, USA. (yuhui@umich.edu; becky@umich.edu)